2024 IEEE International Conference on Robotics and Automation (ICRA 2024)
May 13-17, 2024. Yokohama, Japan

Dynamic Adaptive Imaging System on Optoelectronic Tweezers Platform *

Ao Wang[1], Chunyuan Gan[1], Haocheng Han[1], Hongyi Xiong[1], Jiawei Zhao[1], Chutian Wang[1], Lin Feng[2]*

***Abstract*—Optoelectronic tweezers (OET) has shown great promise in various applications, especially in the precise manipulation of microparticles and microorganisms on a micron and nanometer scale. This technology significantly enhances the efficiency of single-cell sorting and the development of antibody-based drugs. However, conventional OET platforms are limited by issues such as low autofocusing accuracy, restricted imaging field of view, and uneven illumination. To overcome these limitations, we have innovatively developed a dynamic adaptive imaging system. By incorporating peak-finding and in situ Gaussian blur compensation algorithms, we achieved rapid automatic focusing and illumination shadow compensation across an expanded field of view. At the same time, the system can also dynamically adjust compensation parameters under different lighting conditions. Our system has successfully completed comprehensive scanning of the optoelectronic tweezers chip, achieving a 60% reduction in autofocus time and a 15.8% improvement in lighting uniformity. Moreover, this imaging system demonstrates robust versatility and can serve as a reference for other optical systems.**

I. Introduction

Optoelectronic Tweezers (OET) are an advanced manipulation methodology that combines optical tweezers[1] with dielectrophoresis. By irradiating photosensitive materials with optical patterns, virtual photopatterned electrodes are formed. These electrodes generate non-uniform electric fields capable of manipulating cells, microbes, and microparticles[2]. The light-induced dielectrophoresis effect can achieve greater control force under lower light intensity compared to traditional optical tweezers. Unlike traditional optical tweezers, OET obviates the need for high-power laser sources and eliminates potential damage to targets from Joule heating. As a result, OET shows considerable promise in applications ranging from microrobot control[3] and micro-to-nano scale electrode fabrication[4] to biotechnological research[5]. Furthermore, several derivative technologies based on optical tweezers can be transferred to the OET platform, presenting significant potential for further applications. Examples include dynamic force sensing technologies[6], in-situ manufacturing and manipulation techniques [7].

This work was supported by the Beijing Municipal Fund for Distinguished Young Scholars (Grand No. JQ22022), National Key R&D Program of China (Grant No. 2022YFF1502000).

[1]Ao Wang, Chunyuan Gan, Haocheng Han, Hongyi Xiong, Jiawei Zhao, Chutian Wang, are with School of Mechanical Engineering & Automation, Beihang University, Beijing 100083, China(e-mail: aowang@buaa.edu.cn)

[2]Lin Feng is with Beihang University; Beijing Advanced Innovation Center for Biomedical Engineering and Schol of Mechanical Engineering & Automation, Beijing 100083, China.

* Correspondence: linfeng@buaa.edu.cn Lin Feng.

The microfluidic technology leveraging Optoelectronic Tweezers enables high-throughput and precise manipulation of single cells or microparticles[8]. Liu et al. proposed a real-time path planning system to achieve precise cluster control of 3T3 cells [9].Yang et al. introduced the self-locking optical tweezers (SLOT), a novel OET platform featuring an array of optically tunable phototransistor traps that addresses previous limitations by allowing for high-throughput, massively parallel trapping and manipulation in high conductivity media, while maintaining high cell viability and scalability[10]. Hsu et al. introduced a phototransistor-based Optoelectronic Tweezers (Ph-OET) with significantly higher photoconductivity than conventional amorphous silicon-based systems, enabling efficient trapping and manipulation of live cells in high-conductivity media like PBS and DMEM, and offering precise, real-time control for single-cell studies [11].

One of the significant factors affecting the efficiency of cell manipulation is the field of view on the OET platform; a larger field of view correlates with increased operational efficiency. Nonetheless, an expanded view often results in image illumination non-uniformity, stemming from the inherent optical properties of the objective lens. Moreover, each time the OET chip is repositioned, manual refocusing by the operator is generally required. Conventional autofocus algorithms struggle to pinpoint the central channel layer of the three-layer OET microchannel chip accurately. Addressing these challenges, this paper introduces a dynamic adaptive imaging system specifically designed for OET platforms. The system can automatically focus on the middle channel layer without necessitating additional external hardware or intricate image recognition algorithms. Coupled with in situ shadow compensation based on Gaussian blur, the system allows for large-field view scanning and automatic image splicing.

II. System Construction

A. OET Manipulation Platform

The optical system of the OET manipulation platform is shown in Fig.1(a) schematically. This optical system comprises projection, illumination, and observation pathways. The projection pathway is formed by a DMD projector (TI DLP6500) coupled with a projection lens, while the observation pathway consists of a 4X objective lens (Olympus UPLFLN4X), a tube lens (SWTLU-C), and a 4K CCD camera (LBAS U3120-23C). The DMD projector connects to a computer to project light patterns onto the OET chip. Concurrently, the same objective lens is used for both projecting and observing. Optimal illumination is achieved by fine-tuning the positioning of the two convex lenses. The AC power supply and microfluidic inlet are integrated into the chip fixture. This design allows AC power to be delivered to

the OET chip's top and bottom electrodes through metal probes, creating a specific AC signal for the chip. Fig.1(b) depicts the prototype of the OET manipulation platform. The foundation of this system includes an XYZ moving stage used for positioning the chip and autofocusing. Additionally, a syringe pump injects cells or microparticles into the OET chip through PTFE tubing.

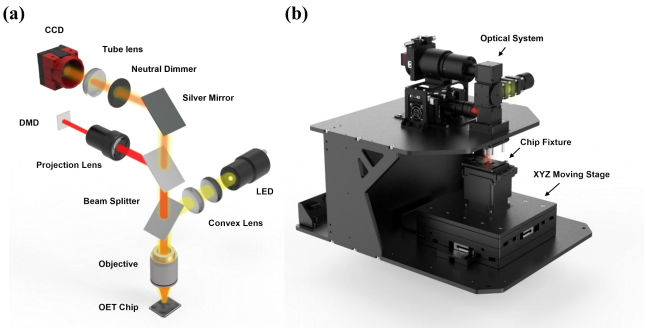

Figure 1. (a) The optical system of the OET manipulation platform. (b) The prototype of OET platform.

B. OET chip

Fig.2 illustrates the architecture of the OET chip, which consists of a tri-layer structure: top, middle, and bottom layers. The top electrode layer is fabricated from 0.7 mm-thick transparent glass coated with a 200 nm layer of indium-tin oxide (ITO). This layer features two through-holes, each with a 1.5 mm diameter, situated on either side of the top glass plate to facilitate solution perfusion and outflow. The bottom layer is constructed from 1 mm-thick ITO glass overlaid with a 1 μm-thick layer of hydrogenated amorphous silicon (a-H:Si), deposited via plasma-enhanced chemical vapor deposition (Leeliven Instruments Hassrode Shale)[12]. The middle layer, with a thickness of 35μm, is crafted using a negative-type photoresist (SU-8 3025, Microchem). A lithography machine (URE 2000S) is employed to create hundreds of microchambers through a process of exposure, development, and rinsing. These chambers measure 30 μm in width and 125 μm in length. Lastly, the assembled tri-layer structure undergoes oxygen plasma treatment (SAOT YZD08-2C) for 30 seconds and is thermally bonded at 90°C for 20 minutes[13]. It is important to note that the upper and lower layers of the OET chip are offset by 2.5 mm to allocate contact points for the metal probes.

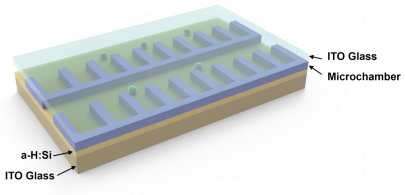

Figure 2. The structure of the OET chip.

III. Assessment of Autofocus Algorithms

For enhanced precision in microparticle manipulation using OET, obtaining a high-quality microscopic image is critical. Manual focusing methods are not only time-consuming and labor-intensive but also inefficient. Therefore, the integration of an autofocus system is imperative. Autofocus can be divided into active and passive methods [14]. Active focusing involves capturing and analyzing the position information of the target object via signals sent from specialized equipment. Conversely, passive focusing centers on the analysis of light reflected off the target object or its pattern information.

The focusing method based on image processing is a passive focusing method. It quantitatively gauges image defocus through a sharpness evaluation function and iteratively adjusts the focal length according to the defocus level until optimal focus is achieved. Compared to other focusing techniques, this image processing-based autofocus method exhibits the following distinctive features:

- The method enables a quantitative assessment of target image sharpness via a focus evaluation operator, boasting both high practical utility and flexibility.
- It relies on computational algorithms rather than specialized measurement equipment for autofocus, thereby reducing system costs.
- The computer-based image recognition outperforms human visual assessment, particularly for images near the quasi-focus plane, facilitating the identification of optimally focused images.

A. Sharpness Evaluation Function

The choice of an appropriate image sharpness evaluation function serves as a critical factor in the success of the autofocus algorithm. A well-focused image inherently possesses greater clarity and detail compared to a defocused one, characterized by a higher gradient value in the spatial domain and richer high-frequency components in the frequency domain. An effective sharpness evaluation function should offer robust resistance to noise, unbiased performance, high sensitivity, and fast calculation speed[15]. In this study, we explored and assessed eight different sharpness evaluation functions, each designed based on one of three main domains: frequency, spatial, and statistical features.

- Sobel: Utilizing two 3×3 directional templates —horizontal and vertical—Sobel operators conduct neighborhood convolutions for each pixel within an image. These directional templates specifically detect vertical and horizontal edges. Additionally, the Sobel function enhances the weights of the four cardinal directions—up, down, left, and right—surrounding the center pixel, thus affording a degree of noise suppression. The corresponding mathematical expression for this operation is detailed below:

$$F_{SOB} = \sum_{x}\sum_{y} |S_1 \otimes f(x,y) + S_1 \otimes f(x,y)| \tag{1}$$

$$S_1 = \begin{bmatrix} -1 & 0 & 1 \\ -2 & 0 & 2 \\ -1 & 0 & 1 \end{bmatrix} \quad S_2 = \begin{bmatrix} -1 & -2 & -1 \\ 0 & 0 & 0 \\ 1 & 2 & 1 \end{bmatrix} \tag{2}$$

Where S_1 is the horizontal template and S_2 is the vertical template and $f(x,y)$ is the gray level of pixel located at coordinates x,y.

- Tenegrad (TEN): This algorithm convolves an image with Sobel operators, and then the square of all the magnitudes greater than a threshold value was summed[16]. The expression is:

$$F_{TEN}=\sum_x\sum_y[S(x,y)]^2\ ,\ S(x,y)>T \tag{3}$$

In the formula, $S(x,y)$ represents the convolution of pixel (i,j) in the image with the Sobel operator, and the expression is as follows:

$$S(x,y)=\sqrt{G_1^2(x,y)+G_2^2(x,y)} \tag{4}$$

- Variance of the image(VAR): A sharply focused image has a greater grayscale difference between each pixel, so the evaluation function can be constructed by calculating the variance or standard deviation of the image[17]. The calculation formula of the variance function is as follows:

$$F_{VAR}=\sum_x\sum_y[f(x,y)-\frac{1}{MN}\sum_x\sum_y f(x,y)]^2 \tag{5}$$

where N and M denote the dimensions of the image in terms of the number of pixels along its length and width, respectively.

- Energy of the image(ENE): The energy gradient function first calculates the difference between the gray values of adjacent pixels in the x direction and the y direction, then calculates the sum of the squares in these two directions. The expression of the energy gradient function is as follows:

$$F_{ENE}=\sum_x\sum_y\{f(x+1,y)-f(x,y)]^2+[f(x,y+1)-f(x,y)]^2\} \tag{6}$$

- Brenner(BRE): Commonly referred to as the Gradient Filter Algorithm, the Brenner Function is the most rudimentary gradient evaluation function. Compared with the previously discussed functions, it exclusively considers the grayscale gradient variation along the x-axis and calculates the gradient difference across two adjacent pixels. Given that the function incorporates a squaring operation, the impact of edge features is accentuated. The mathematical formulation for the Brenner Function is delineated below:

$$F_{BRE}=\sum_x\sum_y[f(x+2,y)-f(x,y)]^2 \tag{7}$$

- Laplacian(LAP): Use the Laplace operator L to perform grayscale convolution calculations on each pixel of the image, and calculate the sum of squares of the convolution to obtain the evaluation function:

$$F_{LAP}=\sum_x\sum_y[L\otimes f(x,y)]^2 \tag{8}$$

$$L=\begin{bmatrix}-1&-1&-1\\-1&8&-1\\-1&-1&-1\end{bmatrix} \tag{9}$$

- Midfrequency-Discrete cosine transform(MDCT): The effect of the band-pass DCT coefficients on the focus measure has been analyzed by[18]:

$$F_{MDCT}=\sum_x\sum_y(f(x,y)\otimes O_{MDCT})^2 \tag{10}$$

$$O_{MDCT}=\begin{bmatrix}1&1&-1&-1\\1&1&-1&-1\\-1&-1&1&1\\-1&-1&1&1\end{bmatrix} \tag{11}$$

- Vollath's F4(VOL): The Vollaths function is based on autocorrelation, which quantifies the spatial similarity between two points [19]. In a sharply focused image, the edges present a stark contrast against the background, resulting in weaker pixel correlations. Conversely, a blurred image features less distinct boundaries, leading to stronger pixel correlations. Accordingly, the peak of the Vollaths Function curve for a focused image appears sharper, while that for a blurred image manifests as more gentle. The mathematical expression for the Vollaths Function is as follows:

$$F_{VOL}=\sum_x^{M-1}\sum_y^N f(x,y)f(x+1,y)-\sum_x^{M-2}\sum_y^N f(x,y)f(x+2,y) \tag{12}$$

B. *Autofocus Workflow*

The autofocus workflow proceeds as follows: As shown in Fig.3, initially, the LED light source intensity is adjusted, and the CCD camera is set to auto-exposure and auto-gain modes. Next, the motion platform moves at a constant speed over a predetermined distance from its starting point. Throughout this movement, real-time calculations are performed using the image sharpness evaluation function, with both the function values and corresponding motion platform position values being recorded. A peak-finding algorithm is then employed [20] to identify the first and second peaks of the sharpness evaluation curve, signifying the upper and lower surfaces of the OET chip's middle layer, respectively. The optimal focus position of the OET chip is determined by calculating the position of the trough between these two peaks[21]. Concurrently, the distance difference between these peaks is used to quantify the thickness of the middle layer of the OET chip.

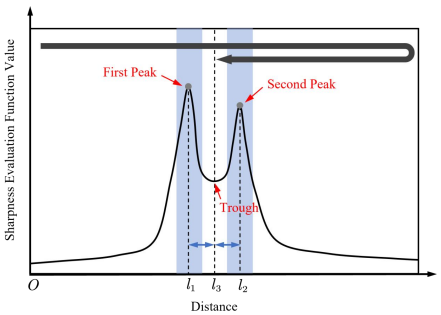

Figure 3. Schematic diagram of autofocus workflow. The position of the trough is the best focus position of the OET chip.

C. *Autofocus Algorithms Comparison*

To assess the autofocus efficacy of various sharpness evaluation algorithms, we initially manually focused the OET system to its optimal position. We then lowered the Z-axis platform by 0.5 mm to establish the autofocus algorithm's starting point for the autofocus algorithm and proceeded to ascend by 1 mm at a rate of 20 μm/s. Concurrently, the CCD camera captured images at a rate of 10 frames per second, and data from eight distinct sharpness evaluation algorithms were recorded. As depicted in Fig. 4, under consistent lighting conditions and OET chip positions, the normalized values for these algorithms were compared. Most algorithms displayed a bimodal behavior, with the exception of the VAR algorithm. Notably, the second peaks of the BRE, LAP, and MDCT algorithms were significantly smaller than their first peaks, posing a challenge for the peak-finding algorithm to identify the intervening trough. It is worth noting that the trough between the double peaks of the SOB algorithm displays a high value, which can render the algorithm susceptible to factors such as noise. Additionally, the average separation between the double peaks was measured at 32.6 μm, closely approximating the actual thickness of the OET chip's middle layer at 35 μm. This suggests that the autofocus algorithm can also serve as a tool for measuring interlayer thickness.

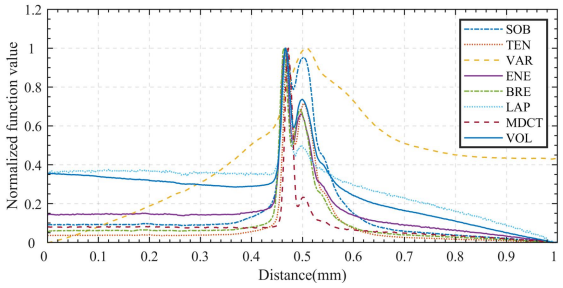

Figure 4. Normalized value of different Sharpness evaluation functions

For real-time applications, it is essential to strike a balance between computational time and accuracy. We recorded the average computation time for various sharpness evaluation algorithms on images with a resolution of 4096×3000, as depicted in Fig. 5. Notably, the VAR method emerged as the fastest, clocking in at 12.1 ms per image, while the TEN method was the most time-consuming, taking 72.3 ms per image

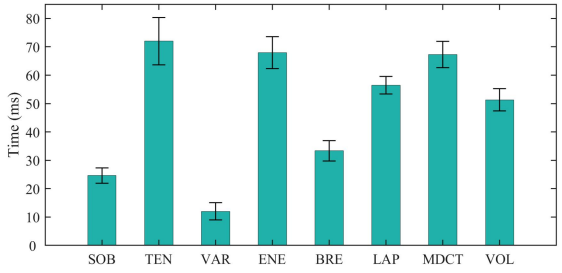

Figure 5. Averaged computation time of single image processed by different focus evaluation functions.

As shown in Fig. 6, we evaluated the autofocus accuracy of various algorithms under different lighting conditions. The brightness in the bright state is twice that of the brightness in the dark state. Initially, we manually focused the OET chip and noted the Z-axis position of the motion platform. Subsequent autofocus tests were conducted using eight sharpness evaluation algorithms along with a bimodal search algorithm. The data reveal that all algorithms experience diminished autofocus accuracy in low-light conditions. Notably, the VAR method is ineffective for autofocusing the OET chip due to the absence of a double-peak phenomenon. Additionally, the SOB and BRE algorithms exhibit a significant drop in autofocus accuracy under varied lighting conditions.

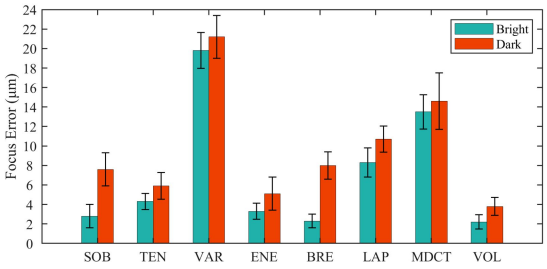

Figure 6. Mean error for each autofocus algorithm under bright and dark light conditions.

Overall, the VOL algorithm demonstrates good focusing accuracy under various lighting conditions, and its computation time is acceptable compared to other algorithms, making it the recommended choice for focusing tasks. The BRE algorithm offers shorter computation times than the VOL algorithm but is more significantly affected by lighting conditions. In situations where lighting conditions are sufficient, the BRE algorithm also represents a viable option.

IV. Image Shadow Compensation

The OET manipulation platform provides the ability for extended observations of micro-objects like cells over a wide field. This requires detailed scanning and stitching together of images across the chip. However, a ubiquitous challenge in such optical systems is the non-uniform illumination at the edges of the objective lens, known as ‘vignetting’. Current microscopy imaging shadow compensation methodologies can broadly be categorized into two major types: retrospective and prospective.

Retrospective methods utilize actual sample images to estimate illumination bias directly. Single-image retrospective methods rely solely on the image to be compensated for estimating the illumination gain[22]. Multi-image approaches involve capturing a large dataset of sample images to learn and establish a shadow compensation model. Theoretically, this method can address any issues of non-uniform illumination. However, model-based approaches are sensitive to sample quality; when the sample has limited blank areas, the compensation outcome is suboptimal [23].

Prospective methods are considered to be the most reliable approaches for image shadow compensation. For bright-field microscopy systems, typical methods for acquiring a reference image include capturing an empty glass slide, culture dish, or

microfluidic chip. Dividing the original image by the reference image yields the shadow-compensated image. However, these methods come with certain limitations. Firstly, blank reference images are inevitably contaminated with imperfections such as dust particles, impurities, or manufacturing defects, which introduce random shadows into the reference image, thereby compromising the quality of the subsequent shadow compensation [24]. Secondly, in practical applications, lighting conditions are rarely static. Any alteration in optical parameters necessitates the re-acquisition of a blank reference image, posing a considerable inconvenience.

Our system employs an enhanced prospective method. Initially, an image is captured at a position on the microfluidic chip devoid of channels, serving as a white reference image, termed the 'original mask' (Fig. 7(a)). Due to contaminants like dust, impurities, or manufacturing defects, the original mask inevitably contains localized noise and blemishes. Low-pass filtering techniques can be employed to eliminate such noise. This filtering is typically achieved by convolving the image $p(x)$ with a Gaussian kernel. The Gaussian function $G(x,y)$ is defined as follows:

$$G(x,y) = \frac{1}{2\pi\sigma^2}\exp[-(x^2+y^2)/2\sigma^2] \tag{13}$$

Here, σ defines the effective spread of the function. The function serves to delineate spatial frequencies within the image, resulting in a trade-off between edge sharpness and intensity averaging. A larger value of σ produces greater smoothing effects.

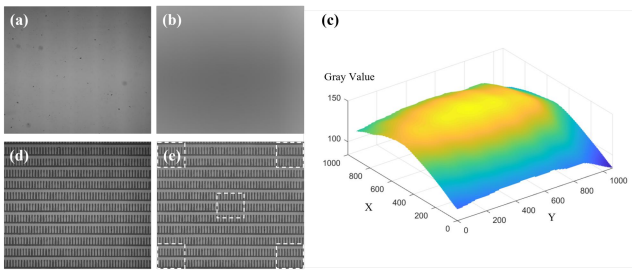

Figure 7. Shadow compensation process. (a) The original mask. (b) The compensation mask. (c) The grayscale value of compensation mask. (d) The image to be shadow compensation. (e) The image after shadow compensation.

After applying Gaussian blurring, the original mask is inverted to black and white. The maximum and minimum grayscale values of the image are determined. By subtracting the minimum value from every pixel in the inverted image, a compensation mask is obtained (Fig.7 (b)). In Fig.7 (c), X and Y represent the pixel values of the compensated mask. It is evident that the central part of the optical image has a noticeably higher gray value than the surrounding area. This compensation mask is then superimposed onto the image to be compensated, yielding a corrected image. It should be noted that the effectiveness of shadow compensation is highly sensitive to the value of σ in the Gaussian filter. To achieve optimal compensation results, we propose an evaluation function for compensation effectiveness. First, the average grayscale values at the four corners of the compensated image are computed based on the dimensions of the image(Fig.7 (e)). This value is then divided by the average grayscale value in the central region of the image and subtracted by one. The V value closer to zero indicates better shadow compensation. If the V value is greater than zero, the compensation is overly aggressive; if less than zero, shadowing still persists.

$$V = \frac{c_1 + c_2 + c_3 + c_4}{4 \cdot c_5} - 1 \tag{14}$$

Here, variables c_1 , c_2 , c_3 , and c_4 denote the average grayscale values of the four corner regions of the image, respectively. c_5 represents the average grayscale value of the central region of the image.

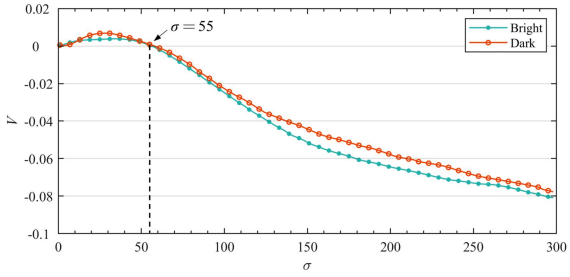

Figure 8. The change curve of V with σ under light and dark lighting conditions.

As illustrated in the Fig.8, we plot the curve showing the variation of V values as σ changes from 1 to 300 under both bright and dark lighting conditions. When σ is set to 1, the V values is zero, which can be attributed to the fact that the original mask was applied directly to image compensation without undergoing Gaussian blurring. In this case, the noise present in the original mask is not effectively suppressed, rendering σ=1 a non-meaningful reference point. Upon comparison, we find that at σ=55, the V value is closest to zero. Therefore, σ=55 is chosen as the optimal parameter for Gaussian compensation.

After performing image shadow compensation, it is necessary to evaluate the effectiveness of the compensation. The evaluation criteria for image brightness uniformity are as follows:

$$Q = \frac{\sum|\bar{f} - f(x,y)|}{M \cdot N} \tag{15}$$

Where Q represents the uniformity of image brightness, with a lower value indicating greater uniformity in image brightness. $\bar{f}$ denotes the average grayscale value of the image.

V. Experiments And Results

The overall length of the OET chip is 20 mm, and its width is 16 mm. The single field of view size of the imaging system is 3.6mm×3.2mm. We divided the chip into 30 areas, and the system scans the entire chip according to an 'S' shape pattern. Autofocus, based on the VOL algorithm, is performed each time it moves to a new field of view, taking an average of 3.5 seconds for a single focus. To benchmark the autofocus time, we enlisted five volunteers skilled in operating optical microscopes to manually control the Z-axis motion platform for focusing. Each volunteer conducted three sets of experiments under uniform lighting conditions. The final average focusing time, calculated from all data collected, was 5.8 seconds for manual focus. Thus, the efficiency of this

system has improved by 60%. After achieving focus, shadow compensation is applied to the image. The average uniformity of image brightness before and after shadow compensation improved from Q=26.5 and Q=22.3, respectively, indicating an approximate 15.8% enhancement in image brightness uniformity. As demonstrated in Fig. 9, noticeable shadows are present at the seams of adjacent domains before shadow compensation. Post-compensation, these shadows are essentially eliminated. This improvement suggests that in the future, we will be able to quantitatively compare cell growth status through cells' fluorescence response, facilitating the identification of specific cells.

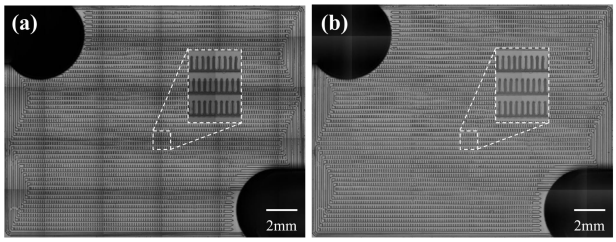

Figure 9. (a) Full scanned image before automatic processing (b) Full scanned image after automatic processing.

VI. Conclusion

In this study, we introduce a dynamic adaptive system specifically tailored for the OET manipulation platform. We conducted a comprehensive evaluation of multiple autofocus algorithms under varying lighting conditions—both bright and dim. Considering both accuracy and computational efficiency, we recommend the use of either the Vollaths (VOL) or Brenner (BRE) algorithms to achieve optimal focus. Furthermore, the system incorporates an in situ image illumination compensation method based on Gaussian blurring. This technique is capable of adapting to different lighting conditions and dynamically calculating mask compensation parameters (σ) for OET chips with various structures. Consequently, the developed system represents a step forward in facilitating the unmanned operation of OET platforms, thereby enhancing experimental efficiency.

Acknowledgment

The authors acknowledge the support from Xiaoyang Chang and the Center for Micro-Nano Innovation at Beihang University (Beihang Nano) for help with device fabrication.

References

[1] A. Ashkin, J. M. Dziedzic, and T. Yamane, "Optical trapping and manipulation of single cells using infrared laser beams," *Nature,* vol. 330, no. 6150, pp. 769-771, 1987.

[2] P. Y. Chiou, A. T. Ohta, and M. C. Wu, "Massively parallel manipulation of single cells and microparticles using optical images," *Nature,* vol. 436, no. 7049, pp. 370-2, Jul 21, 2005.

[3] W. Liang, L. Liu, J. Wang, X. Yang, Y. Wang, W. J. Li, and W. Yang, "A Review on Optoelectrokinetics-Based Manipulation and Fabrication of Micro/Nanomaterials," *Micromachines (Basel),* vol. 11, no. 1, Jan 10, 2020.

[4] S. Zhang, W. Li, M. Elsayed, J. Peng, Y. Chen, Y. Zhang, Y. Zhang, M. Shayegannia, W. Dou, T. Wang, Y. Sun, N. P. Kherani, S. L. Neale, and A. R. Wheeler, "Integrated Assembly and Photopreservation of Topographical Micropatterns," *Small,* vol. 17, no. 37, pp. e2103702, Sep, 2021.

[5] S. Zhang, B. Xu, M. Elsayed, F. Nan, W. Liang, J. K. Valley, L. Liu, Q. Huang, M. C. Wu, and A. R. Wheeler, "Optoelectronic tweezers: a versatile toolbox for nano-/micro-manipulation," *Chem Soc Rev,* vol. 51, no. 22, pp. 9203-9242, Nov 14, 2022.

[6] Y. Huang, P. Cheng, and C. H. Menq, "Dynamic Force Sensing Using an Optically Trapped Probing System," *IEEE ASME Trans Mechatron,* vol. 16, no. 6, Dec 1, 2011.

[7] F. Dawood, S. Qin, L. Li, E. Y. Lin, and J. T. Fourkas, "Simultaneous microscale optical manipulation, fabrication and immobilisation in aqueous media," *Chemical Science,* vol. 3, no. 8, 2012.

[8] S. Liang, Y. Cao, Y. Dai, F. Wang, X. Bai, B. Song, C. Zhang, C. Gan, F. Arai, and L. Feng, "A Versatile Optoelectronic Tweezer System for Micro-Objects Manipulation: Transportation, Patterning, Sorting, Rotating and Storage," *Micromachines (Basel),* vol. 12, no. 3, Mar 6, 2021.

[9] J. Liu, H. Wang, M. Liu, R. Zhao, Y. Zhao, T. Sun, and Q. Shi, "POMDP-Based Real-Time Path Planning for Manipulation of Multiple Microparticles via Optoelectronic Tweezers," *Cyborg Bionic Syst,* vol. 2022, pp. 9890607, 2022.

[10] Y. Yang, Y. Mao, K. S. Shin, C. O. Chui, and P. Y. Chiou, "Self-Locking Optoelectronic Tweezers for Single-Cell and Microparticle Manipulation across a Large Area in High Conductivity Media," *Sci Rep,* vol. 6, pp. 22630, Mar 4, 2016.

[11] H. Y. Hsu, A. T. Ohta, P. Y. Chiou, A. Jamshidi, S. L. Neale, and M. C. Wu, "Phototransistor-based optoelectronic tweezers for dynamic cell manipulation in cell culture media," *Lab Chip,* vol. 10, no. 2, pp. 165-72, Jan 21, 2010.

[12] S. Zhang, Y. Liu, Y. Qian, W. Li, J. Juvert, P. Tian, J.-C. Navarro, A. W. Clark, E. Gu, M. D. Dawson, J. M. Cooper, and S. L. Neale, "Manufacturing with light - micro-assembly of opto-electronic microstructures," *Optics Express,* vol. 25, no. 23, 2017.

[13] W. Zhang, B. Song, X. Bai, J. Guo, L. Feng, and F. Arai, "A portable acoustofluidic device for multifunctional cell manipulation and reconstruction." pp. 664-669.

[14] J. M. Castillo-Secilla, M. Saval-Calvo, L. Medina-Valdes, S. Cuenca-Asensi, A. Martinez-Alvarez, C. Sanchez, and G. Cristobal, "Autofocus method for automated microscopy using embedded GPUs," *Biomed Opt Express,* vol. 8, no. 3, pp. 1731-1740, Mar 1, 2017.

[15] M. Bonet Sanz, F. Machado Sanchez, and S. Borromeo, "An algorithm selection methodology for automated focusing in optical microscopy," *Microsc Res Tech,* vol. 85, no. 5, pp. 1742-1756, May, 2022.

[16] R. Redondo, G. Bueno, J. C. Valdiviezo, R. Nava, G. Cristobal, O. Deniz, M. Garcia-Rojo, J. Salido, M. Fernandez Mdel, J. Vidal, and B. Escalante-Ramirez, "Autofocus evaluation for brightfield microscopy pathology," *J Biomed Opt,* vol. 17, no. 3, pp. 036008, Mar, 2012.

[17] F. C. Groen, I. T. Young, and G. Ligthart, "A comparison of different focus functions for use in autofocus algorithms," *Cytometry: The Journal of the International Society for Analytical Cytology,* vol. 6, no. 2, pp. 81-91, 1985.

[18] L. Sang-Yong, Y. Kumar, C. Ji-Man, L. Sang-Won, and K. Soo-Won, "Enhanced Autofocus Algorithm Using Robust Focus Measure and Fuzzy Reasoning," *IEEE Transactions on Circuits and Systems for Video Technology,* vol. 18, no. 9, pp. 1237-1246, 2008.

[19] A. Santos, C. ORTIZ DE SOLÓRZANO, J. J. Vaquero, J. M. Pena, N. Malpica, and F. del Pozo, "Evaluation of autofocus functions in molecular cytogenetic analysis," *Journal of microscopy,* vol. 188, no. 3, pp. 264-272, 1997.

[20] F. Scholkmann, J. Boss, and M. Wolf, "An efficient algorithm for automatic peak detection in noisy periodic and quasi-periodic signals," *Algorithms,* vol. 5, no. 4, pp. 588-603, 2012.

[21] G. Palshikar, "Simple algorithms for peak detection in time-series."

[22] F. W. Leong, M. Brady, and J. O. D. McGee, "Correction of uneven illumination (vignetting) in digital microscopy images," *Journal of clinical pathology,* vol. 56, no. 8, pp. 619-621, 2003.

[23] J. Yu, J. Zhao, H. Shao, Y. Lu, Y. He, and L. Zhang, "Illumination compensation for microscope images based on illumination difference estimation," *The Visual Computer,* vol. 38, no. 5, pp. 1775-1786, 2021.

[24] S. Singh, M. A. Bray, T. Jones, and A. Carpenter, " Pipeline for illumination correction of images for high-throughput microscopy, " *Journal of microscopy,* vol. 256, no. 3, pp. 231-236, 2014.